Available online at www.sciencedirect.com
SCIENCE DIRECT
Journal of Magnetic Resonance 178 (2006) 121–128
JMR Journal of Magnetic Resonance
www.elsevier.com/locate/jmr

Application of the chirp z-transform to MRI data

J. Kaffanke [a], T. Dierkes [a], S. Romanzetti [a], M. Halse [b], J. Rioux [b], M.O. Leach [c], B. Balcom [b], N.J. Shah [a,d,*]

[a] Institute of Medicine, Research Centre Jülich, D-52425 Jülich, Germany
[b] Department of Physics, MRI Centre, P.O. Box 4400, University of New Brunswick, Fredericton, NB, Canada E3B5A3
[c] Cancer Research UK Clinical Magnetic Resonance Research Group, The Institute of Cancer Research and The Royal Marsden NHS Foundation Trust, Downs Road, Sutton, Surrey SM2 5PT, UK
[d] Institute of Physics, University of Dortmund, D-44221 Dortmund, Germany

Received 30 April 2005; revised 7 August 2005
Available online 10 October 2005

Abstract

A version of the chirp z-transform (CZT) enabling signal intensity and phase-preserving field-of-view scaling has been programmed. The algorithm is important for all single-point imaging sequences such as SPRITE when used with multiple data acquisition for T_2^* mapping or signal averaging. CZT has particular utility for SPRITE imaging of nuclei with short relaxation times such as sodium at high field. Here, a complete theory of the properties of CZT is given. This method operates entirely in k-space. It is compared with a conventional interpolation approach that works in image space after the application of a fast Fourier transformation.

Keywords: SPRITE; Multiple point acquisition; Chirp z-transform; Interpolation; FOV scaling; MRI; Single point imaging; SPI

1. Introduction

Single point imaging (SPI) sequences as originally proposed by Emid and Creyghton [1] are pure phase encoding sequences. Following stabilisation of the phase encoding gradients, a broadband RF excitation pulse is applied and a single datum point is acquired after an encoding time, t_p. Compared to conventional sequences such as FLASH or EPI, one of the advantages of SPI methods is that the acquired data are not convolved with the T_2^* decay since each point in k-space is acquired after the same encoding time following excitation. In addition, SPI methods are particularly suited for the acquisition of data from fast-relaxing nuclei. Using SPRITE (single point imaging with T_1 enhancement) as a variant of SPI, introduced by Balcom et al. [2], sequence efficiency is increased and large gradient switching is reduced because SPRITE allows the use of small, stepped changes of the magnetic field gradients. Recently, the SPRITE sequence has been further improved by Halse et al. [3] to allow for centric k-space encoding through the utilisation of spiral and conical trajectories.

By sampling multiple data points following a single excitation pulse, SPI sequences are capable of acquiring data for the calculation of T_2^* maps [4]. However, in the multiple-point SPRITE sequence (m-SPRITE), where data acquisition is performed during constant phase encode gradients, the k-space encoding is different for each acquired datum point and therefore the field-of-view (FOV) changes between successive points. With a changing FOV, the signal per voxel scales proportionally with the voxel volume. Hence, FOV scaling and normalisation of image intensity is needed to ensure that the signal intensity per voxel volume is preserved. This can be performed by an interpolation step following a conventional Fourier transform, or by using the chirp z-algorithm developed by Rabiner et al. [5]. Tong et al. [6] used the chirp z-transform (CZT) for rotating and shifting NMR images. The CZT can also

* Corresponding author. Fax: +1 49 2461 61 8294.
E-mail address: n.j.shah@fz-juelich.de (N.J. Shah).

1090-7807/$ - see front matter © 2005 Elsevier Inc. All rights reserved.
doi:10.1016/j.jmr.2005.09.002

be implemented to effect a FOV scaling. This was proposed by Heid [7] for the purposes of using the multiple points for signal averaging. In the work of Halse et al. [8] the CZT was first used for T_2^* mapping of *m*-SPRITE data. The work presented here is an in depth evaluation of the CZT algorithm where, we have in addition modified the CZT algorithm such that phase information is preserved and a coherent summation of the transformed images can be used for signal averaging. It has been shown by Rioux [9] that alternative regridding and interpolation methods, as developed by Dutt and Rokhlin [10], are less accurate and more time consuming.

This study investigates the mathematical properties of the two alternative algorithms. A representation formula of the numerical chirp *z*-transform is derived. It is shown that this representation corresponds to a convolution with a periodic sinc kernel.

2. The SPRITE and *m*-SPRITE sequence

The SPRITE sequence, introduced by Balcom et al. [2], was proposed by Beyea et al. [4] as a promising imaging sequence for T_2^* mapping of fast relaxing nuclei such as sodium. SPRITE, being a variant of the single point imaging method, acquires a single phase-encoded datum point after spin excitation and a fixed time delay, t_p. Three-dimensional phase encoding is achieved with magnetic field gradients that remain constant between RF excitation pulse and signal acquisition in each of the three dimensions (Fig. 1). By stepping the ramped gradient, rapid and large switching of the gradients can be avoided. This not only reduces performance demands on the gradient system but also is beneficial for patients who would be exposed to smaller magnetic field changes, $\mathrm{d}B/\mathrm{d}t$, and less acoustic noise. The time between excitation and signal acquisition can be kept small, which is desirable in the case of fast relaxing nuclei, and is only restricted by the maximum gradient strength and the ring down time of the RF coil.

Since the time t_p is fixed, the reconstructed images are not convolved with T_2^* decay. By acquiring several data points per excitation with *m*-SPRITE (Fig. 1), a series of images can be reconstructed and by fitting the signal intensity of a given voxel, the T_2^* value can be obtained. Furthermore, the spin density can be obtained by extrapolation to time $t = 0$. The main problem here is that the FOV changes as encoding time increases, resulting from the changing sampling of the signal in *k*-space where Δk is proportional to t_p. Additionally, the intensity per voxel in the reconstructed image is proportional to the volume so that normalisation is needed to extract the true T_2^* decay.

3. Theory

3.1. Signal in multiple-point SPRITE

Let $\rho(x)$ be the spin density at the spatial coordinate $x \in \mathfrak{R}^3$. The transverse relaxation time at x is denoted by $T_2^*(x)$. The data sets measured at time points $t \geqslant t_0 > 0$ by a standard multiple-point SPRITE sequence can be expressed as

$$\hat{S}(t,g) = \int_{\mathfrak{R}^3} \rho(x) \mathrm{e}^{-t/T_2^*(x)} \mathrm{e}^{-2\pi i g t \cdot x} \,\mathrm{d}x, \quad g \in \mathfrak{R}^3, \tag{1}$$

where we have used the common abbreviation

$$k(t) = tg = \frac{\gamma}{2\pi} \int_0^t G \,\mathrm{d}\tau,$$

$G \in \mathfrak{R}^3$ is the applied gradient strength for a single point, and γ is the gyromagnetic ratio of the nucleus under investigation, e.g., $\gamma = 42.6\,\mathrm{MHz/T}$ for protons. Note that in multiple-point SPRITE measurements both t and g are variable. We confine ourselves to a one-dimensional

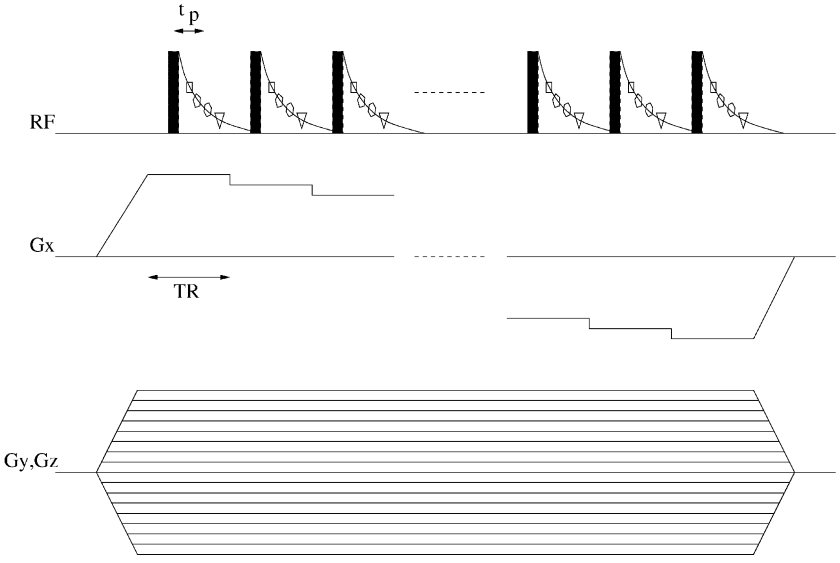

Fig. 1. Schematic representation of the *m*-SPRITE pulse sequence. Note that the data points denoted by different symbols are rebinned to form unique *k*-spaces. This means that a given plane in *k*-space is filled by squares only, pentagons only, and so on.

description for simplicity. Accordingly, we assume that the spin density $\rho(x)$ has finite support in $\Re$,

$$\text{supp } \rho(\mathrm{x}) \subset [-a,a], \quad 0 < 2a = FOV, \tag{2}$$

and the measured signal $\hat{\mathrm{S}}(t,g)$ for $t_0 \leqslant t \leqslant T_R$ and $g_{\min} \leqslant g \leqslant g_{\max}$ is band-limited. Hence, by Shannon's Sampling Theorem [11], we can approximate the SPRITE data $\hat{\mathrm{S}}(t,g)$ to good accuracy by the trapezoidal rule

$$\begin{aligned}\hat{S}(t,g) &\approx \hat{S}_{\text{approx}}(tg)\\ &= \Delta x \sum_{m=-q}^{q-1} \rho_{\Delta x}(m) \mathrm{e}^{-t/T^*_{2,\Delta x}(m)} \mathrm{e}^{-2\pi i m \Delta x \cdot tg},\end{aligned} \tag{3}$$

where, $\Delta x = a/q = 2a/N$ denotes the sampling step-size of $\rho(x)$ and $T_2^*(x)$, i.e., the two unknown functions $\rho(x)$ and $T_2^*(x)$ are discretised with $N = 2q$ points. In the following, we use the substitutions $\rho_m = \rho_{\Delta x}(m) = \rho(m\Delta x)$ and $(T_2^*)_m = T^*_{2,\Delta x}(m) = T_2^*(m\Delta x)$. This allows us to formulate the mathematical problem of SPRITE imaging as follows: from a given measurement signal $\hat{\mathrm{S}}(t,g)$, $t_0 \leqslant t \leqslant T_R$ and $g_{\min} \leqslant g \leqslant g_{\max}$, find $2N$ values ρ_m and $(T_2^*)_m$ such that Eq. (3) holds.

Remark: Eq. (3) only formally resembles the discrete Fourier transformation (DFT) since the variables t and g are independent from each other in a SPRITE measurement. To obtain a valid (discrete) Fourier transformation pair, it is necessary to have only one conjugate variable. Obviously, this condition is violated in a SPRITE measurement with multiple point acquisition. Therefore, the theory of DFT does not apply in this case.

From Eq. (1) together with the limits $-g_{\max} \leqslant g \leqslant g_{\max}$ we may write

$$\hat{S}(t,g) = \chi_{1/|g_{\max}|t}(tg)\hat{F}(g,t), \tag{4}$$

where, we have set

$$F(x,t) := \rho(x)\mathrm{e}^{-t/T_2^*(x)},$$

and χ is the indicator function of the interval $[-|g_{\max}|t, |g_{\max}|t]$. The Fourier transform of F is taken w.r.t. the spatial variable x only. Eq. (4) enables us to make use of the formulae in Appendix A after having discretised the measurement signal $\hat{\mathrm{S}}(t,g)$ with respect to both time t and gradient g. This is described in the next section.

3.2. CZT for SPRITE data

For a real experiment, the semi-discrete formulation of Eq. (3) has to be modified further because it is the signal $\hat{\mathrm{S}}(t,g)$ that is naturally sampled in the measurement process. First of all, let us assume that we can adjust the gradient strength G so that the product tg in Eq. (3) is normalised with respect to t. Therefore, we have to differentiate between the absolute time $t_0 \leqslant t \leqslant t_{\max} = t_{p-1}$ of the actual acquisition time, and the relative time $Z = t/t_{\max} \leqslant 1$ of the gradient factor in what follows. In fact, we will see that Z serves as a scaling factor in the reconstruction process described below.

Next, we chose the Nyquist rate $\Delta k = 1/2a = 1/FOV$ as the gradient step-size Δg (according to the support of ρ and T_2^*) such that

$$\Delta x \Delta k = \frac{a}{q}\frac{1}{2a} = \frac{1}{2q}$$

and we assume that we are given a finite number of time points

$$t_l = t_0 + l\Delta t, \quad l = 0,\ldots,p-1,$$

Δt being the dwell time. Now, we apply the chirp z-transform (A.2) to the sampled signal

$$\begin{aligned}&\hat{S}_{n,l} = \hat{S}(t_l, n\Delta k/t_{p-1}), \quad n = -q,\ldots,q-1,\\ &\quad l = 0,\ldots,p-1.\end{aligned}$$

Using (A.4) from Appendix A we obtain

$$\begin{aligned}\tilde{F}_{m,l} &= Z_l \Delta k \cdot \sum_{n=-q}^{q-1} \hat{S}_{n,l} \mathrm{e}^{\pi i Z_l m n/q}, \quad Z_l = t_l/t_{p-1},\\ &= 2qZ_l\Delta k \cdot \Bigg[F(x,t_l)\\ &\qquad \otimes \sum_j \mathrm{e}^{-\pi i Z_l \Delta k (x - j/Z_l\Delta k)} \mathrm{sinc}_{2\pi q Z_l \Delta k}(x - j/Z_l\Delta k)\Bigg]\left(\frac{m}{2q\Delta k}\right),\end{aligned} \tag{5}$$

where the convolution "$\otimes$" is taken with respect to the spatial variable x only. The variable scaling factor, Z_l, has the effect that the result of the convolution is sampled with a constant step-size, $\Delta x = 1/2q\Delta k$. Even more importantly, the result is renormalised such that the values corresponding to the different time points, t_l, are weighted correctly. Thus, the values $\tilde{F}_{m,l}$ which are the result of CZT applied to the measurement set, $\hat{\mathrm{S}}_{n,l}$, are equidistantly sampled in space, independent of Z_l, and accordingly scaled to the effective step-size. Obviously, this is indispensable for the task of averaging or T_2^* fitting, for example. Furthermore, if we put

$$\begin{aligned}&F_{m,l} = F(m\Delta x, t_l) = \rho_m \mathrm{e}^{-t_l/(T_2^*)_m}, \quad m = -q,\ldots,q-1,\\ &\quad l = 0,\ldots,p-1, \quad \Delta x = \frac{1}{2q\Delta k},\end{aligned}$$

as abbreviation, we see from Eq. (5) that the output of CZT is a convolution of the true object function $F_{m,l}$ and a periodic sinc kernel. This is the characterisation of the error introduced by the numerical CZT.

4. Methods

Imaging experiments were performed on a VARIAN 4 Tesla UNITY INOVA whole body scanner. Two m-SPRITE imaging experiments were used to investigate the properties of the reconstruction algorithms with respect to noise and resolution, respectively. A spherical phantom filled with 400 mM saline solution was used for sodium

imaging and a standard resolution phantom filled with transformer oil, for optimal signal uniformity, was used for proton imaging. The sodium phantom was scanned with 81 time points between 10 and 50 ms after spin excitation with a resulting FOV scaling of 5:1 and a dwell time of 500 μs. The FOV for the last image was 400 mm in each coordinate and the experiment was repeated four times to form an averaged data set. The resolution phantom was imaged with encoding times between 0.2 and 1.0 ms measuring 17 time points at a dwell time of 50 μs. Thus, the FOV scaling was up to a factor 5:1. The size of the FOV was 256 mm isotropic and no averaging was needed in the case of proton imaging. Both data sets had a matrix size of $64 \times 64 \times 32$.

An artificial phantom data set was used for simulations modelled by four concentric Bessel functions in k-space representing a resolution phantom of concentric spheres in image space. The data set consisted of a series of 81 images with a maximal FOV scaling of 5:1 representing an MRI scan with acquisition times between 10 and 50 ms and a dwell time of 500 μs. With reference to this, the k-space data were multiplied with a decay process with a relaxation time of $T_2^* = 15$ ms. To enable a good comparison with the MRI scans, the matrix size was again $64 \times 64 \times 32$.

To validate the consistency of the two methods, the CZT and the linear interpolation approach, a simple but important test was used. By taking the magnitude of the sum of all complex image points per time step, t_ℓ , the centre of k-space can be recalculated according to Fourier transform theory

$$\begin{aligned} \left|\hat{S}(t_\ell, k_n)\right| &= \left|\sum_m F(t_\ell, x_m) \mathrm{e}^{-2\pi i k_n x_m}\right|, \\ \left|\hat{S}(t_\ell, 0)\right| &= \left|\sum_m F(t_\ell, x_m)\right|. \end{aligned} \tag{6}$$

Comparing these values with the measured k-space centre points (zero gradients) the accuracy of the data processing was checked.

For a comparison of the influence on SNR between both reconstruction methods, a summation of the magnitude image points was performed. Because of the triangle inequality

$$\left|\sum_m F(t_\ell, x_m)\right| \leqslant \sum_m |F(t_\ell, x_m)|, \tag{7}$$

it is expected that taking the sum of magnitudes leads to coherent noise summation.

An artificial data set with constant value 1.0 in all positions was used to simulate the PSF for both methods with a matrix size of $32 \times 32 \times 16$ with scaling factors up to 5:1. To measure the PSF of an m-SPRITE scan a phantom of 35 ± 5 μl transformer oil was used and carefully positioned within a single voxel volume off-centre in the FOV. Note that now the FOV was chosen such that the size of this tiny phantom was below the effective voxel size; i.e., the matrix size was again $32 \times 32 \times 16$ with a FOV of $128 \times 128 \times 64$ mm resulting in a nominal voxel size of $4 \times 4 \times 4$ mm for the smallest FOV. The encoding time for nine multiple points was between 0.2 and 1.0 ms with a maximum FOV scaling of 5:1. A total of 24 averages were acquired with the PSF oil phantom plus 24 averages with the supporting foam only. In taking the difference between both averaged data sets the signal of the oil phantom was separated from the background.

All data processing was performed on a Macintosh G5 under MAC OS X. Both simulated data and measurement data were reconstructed with the same algorithm programmed with IDL 6.0. The chirp z-transform was programmed as described here. For linear interpolation, a standard IDL function was used. This was performed in image space and independently in real and imaginary parts after transforming the data using a FFT. The algorithm was chosen as the most simple and standard technique for an initial comparison.

5. Results and discussion

The two reconstruction methods, the CZT and interpolation after FFT, were evaluated with respect to resolution maintenance and SNR, respectively.

In Fig. 2 profiles through the simulated and measured PSF are shown for four different time points and scaling factors of 2.5, 1.66, 1.25, and 1 corresponding to encoding times of 0.4, 0.6, 0.8, and 1.0 ms. As predicted by theory, the PSFs for the interpolation method are, to good approximation, $\chi_{1/b_l} \otimes \chi_{1/b_l}$ whereas the PSFs of CZT are sinc functions. Both the simulations and the measurement results exhibit these properties. The deviation from the analytical sinc function, as given in Eq. (5), is explained by under-sampling effects. All PSFs are multiplied by cubic scaling factors. Note that the amplitude of the measured PSFs is reduced by the T_2^* decay of the transformer oil whereas this is not the case for the simulated PSFs.

Reconstructed images of a simulated resolution phantom data set are depicted in Fig. 3. Fig. 4 shows images of the proton resolution phantom and Fig. 5 the sodium imaging results. For all three data sets, four images from each series of 81 images are shown obtained through reconstruction by the CZT and interpolation after FFT, respectively. These four images are arranged with increasing acquisition time from the upper left to the lower right, i.e., the scaling factors decrease in this order. The images are presented with scaling factors of 2.5, 1.66, 1.25, and 1. For higher scaling factors the spatial resolution is almost completely degraded.

The advantage of the CZT is demonstrated by the images of the resolution phantoms (Figs. 3 and 4) where finer structures are clearly better resolved by the CZT. For comparison, profiles through the images are shown. Comparing the interpolation method with CZT, the latter produces stronger ringing artefacts. These artefacts increase with higher scaling factors. This can be explained by the convo-

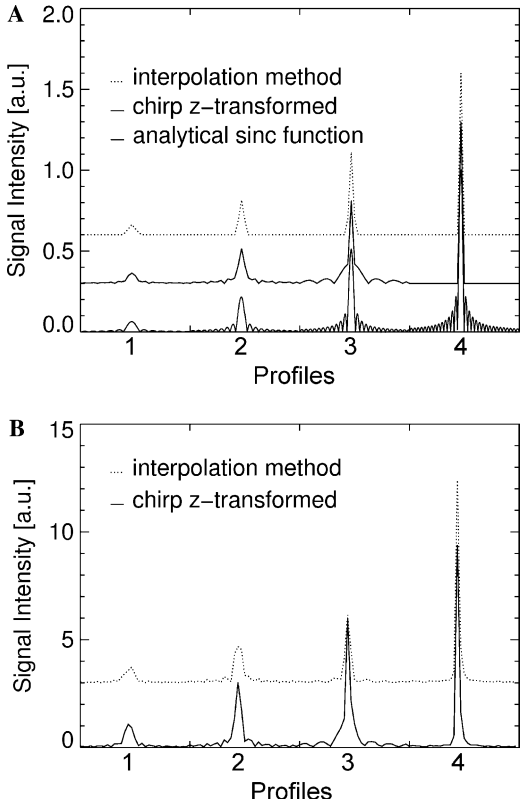

Fig. 2. Four profiles through simulated (A) and measured (B) point spread functions (PSF) are shown for scaling factors of 2.5, 1.66, 1.25, and 1, from left to right. To make the different PSFs distinguishable in one graph artificial offsets of 0.3 and 0.6 (A) and 3.0 (B) have been added to the curves. The simulated PSFs for CZT (solid line) show sinc functions depending on the scaling level both in the simulated PSFs (A) and the measured PSFs (B). The measured PSFs are acquired using a transformer oil phantom with a volume below the voxel size.

lution with sinc functions of decreasing frequency as a property and a drawback of the CZT.

In the case of noisy data sets (e.g., the sodium measurement Fig. 5), the interpolation approach yields images of better SNR compared to the CZT images. It is well known that the interpolation process is almost equivalent to low pass filtering [15].

At higher scaling factors, the noise has a reduced influence since the SNR is a function of the cubic scaling factor. That is, the signal is proportional to the voxel volume with respect to the FFT whereas the noise level is constant for each acquired time point.

A summation of the image point magnitudes according to Eq. (7) results in a coherent summation of the image noise. This provides a simple overall SNR estimate for both methods. Since the constant noise level for all acquired time points is divided by the cubic scaling factor for signal intensity correction, the scaling factor has a significant influence on the sum over magnitudes. Depending on the noise level, the calculated values increase at a certain point in the image series as shown for the sodium images in Fig. 5. With the exception of the last image, where the transformation is identical to

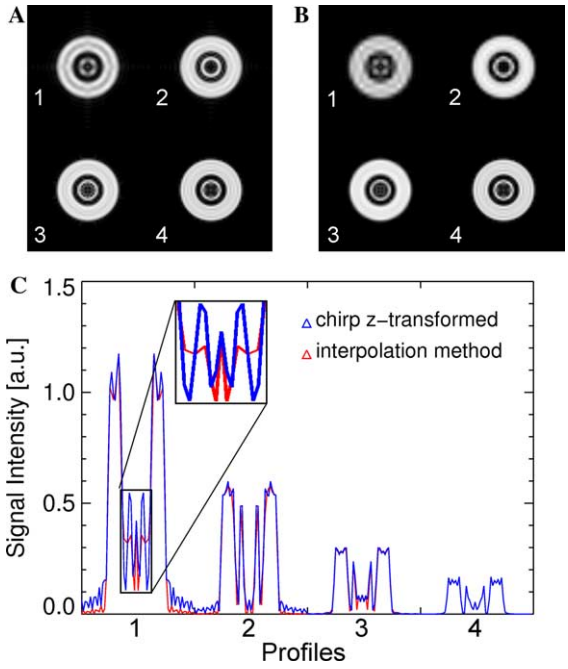

Fig. 3. Simulation results from an artificial resolution phantom modelled by four concentric Bessel functions in *k*-space including (A) CZT and (B) interpolation reconstructions with (C) a comparison of central profiles. Encoding times and scaling factors of 2.5, 1.66, 1.25, and 1 are identical to the proton images in Fig. 4. Central vertical profiles (C) are plotted consecutively from upper left to lower right and each profile consists of 64 pixels. The CZT images exhibit some artefacts in this case.

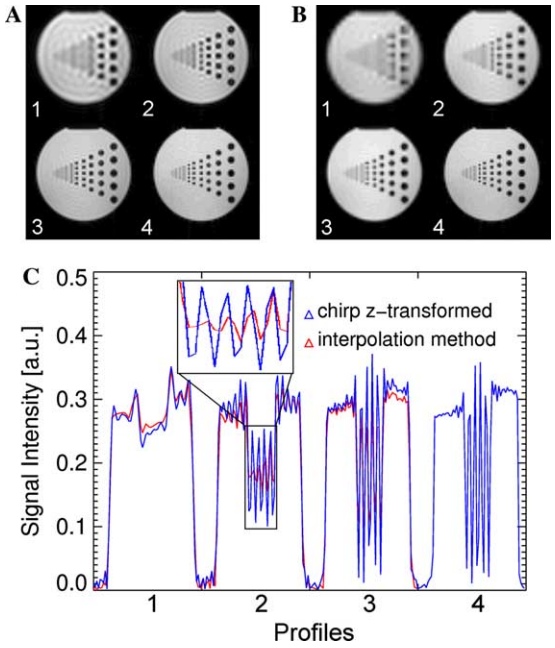

Fig. 4. Results from *m*-SPRITE proton imaging of a resolution phantom filled with transformer oil including (A) CZT and (B) interpolation reconstructions with (C) a comparison of vertical profiles. The CZT reconstructed images (A) show much better resolution compared to the interpolated images after FFT (B). The vertical profiles (C) are plotted consecutively from upper left to lower right and each profile consists of 64 pixels. The encoding times were 0.4, 0.6, 0.8, and 1.0 ms from the upper left to the lower right with corresponding scaling factors of 2.5, 1.66, 1.25, and 1.

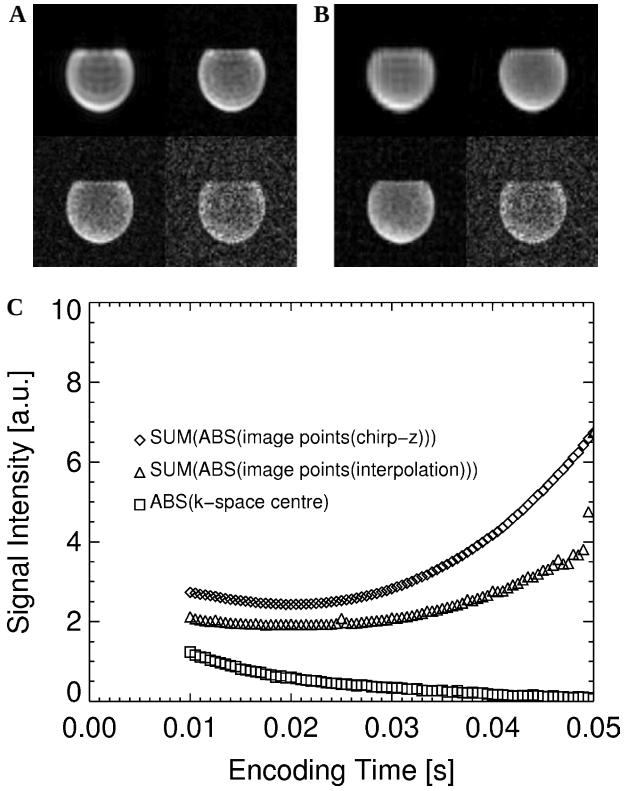

Fig. 5. Results from *m*-SPRITE sodium imaging including (A) CZT and (B) interpolation reconstructions. The CZT reconstructed *m*-SPRITE sodium images (A) appear noisier and less homogeneous compared to the interpolated images after FFT (B). The acquisition times are from the upper left to the lower right 20, 30, 40, and 50 ms with corresponding scaling factors of 2.5, 1.66, 1.25, and 1. (C) The sum over all magnitude points of each image is compared between the CZT reconstructions and the interpolation reconstructions.

the FFT for both data processing models, the chirp *z*-transformed images always result in a higher value, first, because of the convolution with the sinc function in the chirp *z*-transform at higher scaling factors and second, because of the smoothing effect of the interpolation method.

The summation over magnitudes and the difference to the *k*-space centre gives a qualitative measure of the noise level in the images. This calculation serves as an indicator for the feasibility of T_2^* mapping with an acquired data set since T_2^* mapping on a voxel-by-voxel basis needs a sufficient SNR. SNR is reduced not only by relaxation at the end of the decay but also is a function of the scaling factor. A low SNR shifts the voxel signal intensity at the end of the decay curve. This would result in bad fitting results and, consequently, wrong T_2^* values.

An example of the validation procedure as described by Eq. (6) is shown in Fig. 6 for the sodium measurement. The mean relative difference (average ℓ_1-norm) from the *k*-space centre was 4.41% for CZT images and 4.34% for the interpolated images. The good correspondence ensures that the chosen data processing is applicable for T_2^* mapping.

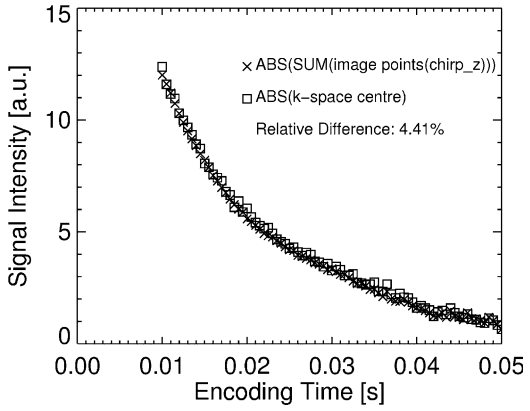

Fig. 6. Comparison of the sum over all complex points for each image reconstructed with CZT and the centre of *k*-space. The data were taken from the sodium imaging scan shown in Fig. 5. The good correspondence demonstrates, in principle, the applicability of CZT in terms of signal preservation.

Note that the local T_2^* decay per voxel must not be confused with the bulk FID, the acquired *k*-space centre, or the recalculated *k*-space centre derived from the CZT images in Fig. 6. The global signal decay of the FID is not identical with the local T_2^* decay in a voxel of finite dimensions since dephasing of transverse magnetisation is different on the global and the local scale.

6. Conclusion

We have shown in our theoretical work that the CZT is the logical reconstruction algorithm for data acquired with an *m*-SPRITE MRI experiment. This follows immediately from the signal equation incorporating the *k*-space acquisition scheme and the scaling with acquisition time. Additionally, we have demonstrated that reconstruction with the CZT is described as a convolution of a sinc function with the correct image. Following the presented theory, we implemented the CZT with the extension of signal normalisation to the voxel volume to be applicable for T_2^* mapping.

Both simulations and MRI data exhibit increasing convolution with sinc functions as the applied scaling factor in the CZT increases. Similar effects of less intensity are recognizable in the interpolated images as well, but must be interpreted as an effect of under-sampling and as a type of ringing artefacts. Interpolation always behaves as a noise filter with a smoothing effect when applied to data sets of low SNR. This property can be beneficial for reconstruction of homogeneous objects but it reduces the resolution of structured objects on the other hand. However, CZT is the superior algorithm in terms of calculation time and is the mathematically correct reconstruction method when FOV scaling is desired. Additionally, CZT can be used as natural point of entry for further filtering. Therefore, we conclude that CZT is the preferable algorithm in most cases where resolution is of primary interest. In such a case, it is strongly recommended to restrict the *m*-

SPRITE MRI experiment to low scaling factors to reduce the artefacts introduced by convolution with the sinc function and also, to preserve the desired resolution as demonstrated in previous work by Halse et al. [8].

Acknowledgments

We gratefully acknowledge support from the Deutsche Forschungsgemeinschaft (ZI 194/14-1) and the Bundesministerium für Bildung und Forschung for support of the 4T MRI facility. We thank Varian GmbH and Varian Inc. for technical support. In particular, we gratefully acknowledge assistance from Michael L. Gyngell, Uwe Köpper and Gerald Simon.

Appendix A

For the benefit of the reader, we briefly list the basic facts of the underlying mathematical theories that are scattered throughout the literature [5,11–15].

We begin with defining the indicator function χ of the unit interval $[-1,1] \subset \Re$

$$\chi(x) = \begin{cases} 1 & \text{for } -1 \leqslant x \leqslant 1, \\ 0 & \text{else.} \end{cases}$$

We have

$$\hat{\chi}(\xi) = \int_{-1}^{1} \mathrm{e}^{-2\pi \mathrm{i} x\xi}\,\mathrm{d}x = \begin{cases} \frac{\sin 2\pi\xi}{\pi\xi}, & \text{if } \xi \neq 0, \\ 2, & \text{if } \xi = 0. \end{cases}$$

which we write as

$$\hat{\chi}(\xi) = 2\mathrm{sinc}(2\pi\xi)$$

for short. For any $a = (a_1, \ldots, a_n) \in \Re^n, \quad a_l > 0$, we also define for $x \in \Re^n$

$$\chi_a(x) := \chi(a_1 x_1) \cdot \chi(a_2 x_2) \cdot \ldots \cdot \chi(a_n x_n)$$

with the corresponding Fourier transform

$$\begin{aligned} \hat{\chi}_a(\xi) &= \frac{1}{|\det A|}\,\hat{\chi}_{(1,\ldots,1)}(A^{-T}\xi) \\ &= \frac{2^n}{|a_1 \cdot \ldots \cdot a_n|}\,\mathrm{sinc}\left(\frac{2\pi\xi_1}{a_1}\right) \cdot \ldots \cdot \mathrm{sinc}\left(\frac{2\pi\xi_n}{a_n}\right), \\ A &= \begin{pmatrix} a_1 & & \\ & \ddots & \\ & & a_n \end{pmatrix} \end{aligned}$$

Now, let our object be a square-integrable function $S \in L^2(\Re^3)$ on $\Re^3$ in image space. We start out from

$$S(x) = \int_{\Re^3} \hat{S}(k)\mathrm{e}^{2\pi \mathrm{i} k\cdot x}\,\mathrm{d}k$$

which gives the imaging equation.

For finite sampling intervals $b_l > 0$, a cut-off at b_l in the k-space coordinates k_l, and $b = (b_1, b_2, b_3)$, results in

$$\begin{aligned} 2^3 b_1 b_2 b_3 [\mathrm{sinc}_{2\pi b} * S](x) &= \int_{\Re^3} \chi_{1/b}(k)\hat{S}(k)\mathrm{e}^{2\pi \mathrm{i} x\cdot k}\,\mathrm{d}k \\ &= \int_{[-b_1,b_1]\times[-b_2,b_2]\times[-b_3,b_3]} \hat{S}(k)\mathrm{e}^{2\pi \mathrm{i} x\cdot k}\,\mathrm{d}k \\ &\doteq \Delta k_1 \Delta k_2 \Delta k_3 \sum_{l=1}^{3} \sum_{j=-q_l}^{q_l-1} \hat{S}_{\Delta k_l}(j)\mathrm{e}^{2\pi \mathrm{i} x_l j \Delta k_l}, \\ \Delta k_l &= b_l/q_l, \end{aligned}$$

where we have approximated the last integral by the trapezoidal rule with a step-size $0 < \Delta k_l = b_l/q_l$, and $2q_l$ is the number of sample points for $\hat{S}$ in each coordinate, respectively.

Having introduced the general form of data sampling, we now use the linear independence of the spatial coordinates and describe only the one-dimensional case in the following for simplicity. Since $[\mathrm{sinc}_{2\pi b} * S]$ is band-limited with precise bandwidth b, the image needs to be sampled with a rate of $\Delta x \leqslant 1/2b = 1/2q\Delta k$. Taking the coarsest possible step-size $\Delta x = 1/2b$, rearranging the last set of equations, and writing out the convolution yields

$$\Delta k \cdot \sum_{j=-q}^{q-1} \hat{S}_{\Delta k}(j)\mathrm{e}^{\pi \mathrm{i} m j/q} \doteq 2b \cdot \int_{\Re} \mathrm{sinc}_{2\pi b}(m/2b - y)S(y)\,\mathrm{d}y,$$
$$m = -q, \ldots, q-1.$$

In the general case, we obtain for an arbitrary sample rate, $\Delta x \leqslant 1/2b = 1/2q\Delta k$, the approximation

$$\Delta k \cdot \sum_{j=-q}^{q-1} \hat{S}_{\Delta k}(j)\mathrm{e}^{2\pi \mathrm{i} m \Delta x j \Delta k} \doteq 2b \cdot \int_{\Re} \mathrm{sinc}_{2\pi q \Delta k}(m\Delta x - y)S(y)\,\mathrm{d}y. \tag{A.1}$$

The concept that leads to the chirp z-transform makes use of the algebraic relation

$$2jm = j^2 + m^2 - (j-m)(j-m)$$

to rewrite the left-hand side as a (discrete) convolution of length $2q$. Setting

$$g(j) := \hat{S}_{\Delta k}(j) \cdot \mathrm{e}^{\pi \mathrm{i} \Delta x \Delta k j \cdot j}$$

and inserting this into the Eq. (A.1) yields

$$S_m = \Delta k \cdot \mathrm{e}^{\pi \mathrm{i} \Delta x \Delta k m \cdot m} \cdot \sum_{j=-q}^{q-1} g(j) \cdot \mathrm{e}^{-\pi \mathrm{i} \Delta x \Delta k (j-m)(j-m)}. \tag{A.2}$$

This equation completely describes the chirp z-transform [5,12,13] and can be performed efficiently by FFT on the order of $q \log q$. Note that we have kept the scaling factor Δk explicit, unlike to the standard definition, given for example in [5]. The reason for doing so here is that we want the approximation by the trapezoidal rule still to be valid. Furthermore, as a result of our derivation we see that the values S_m have the approximate representation

$$S_m \doteq 2b \cdot \int_{\Re} \mathrm{sinc}_{2\pi b}(m\Delta x - y)S(y)\,\mathrm{d}y, \quad \Delta x \leqslant (2b)^{-1} = (2q\Delta k)^{-1} \tag{A.3}$$

if reconstructed by the chirp z-algorithm from the discretely sampled data $\hat{S}_{\Delta k}(j)$ in the finite k-space interval $[-b, b]$. As can be clearly seen from this representation, the parameter Δx acts as a zooming factor whereas the parameter b influences the overall resolution of the chirp z-transform and additionally, causes an intensity scaling.

Finally, if we consider the sampled data $\hat{S}_{\Delta k}(j)$ as a truncated sum of many infinite delta distributions,

$$\hat{S}_{\Delta k}(j) = \chi_{1/b}(k + \Delta k/2) \cdot \sum_j \delta(k - j\Delta k)\hat{S}(k), \quad b = q\Delta k,$$

the result of a discrete Fourier transform (i.e., $\Delta x = 1/2b$) is given by

$$\begin{aligned} S_m &= \Delta k \cdot \sum_{j=-q}^{q-1} \hat{S}_{\Delta k}(j) \cdot \mathrm{e}^{\pi i j \cdot m/q} \\ &= \int_{\Re} \mathrm{e}^{2\pi i k \cdot m\Delta x} \cdot \hat{S}(k) \cdot \chi_{1/b}(k + \Delta k/2) \cdot \sum_j \delta(k - j\Delta k)\,\mathrm{d}k \\ &= 2b \cdot \left[S(x) \otimes \sum_\ell \mathrm{e}^{-\pi i \Delta k (x - \ell/\Delta k)} \cdot \mathrm{sinc}_{2\pi b}(x - \ell/\Delta k) \right](m\Delta x). \end{aligned} \tag{A.4}$$

The second term of the convolution "$\otimes$" (with respect to x) is the analytical expression of the point spread function (PSF) of both the discrete Fourier transform and CZT.

References

[1] S. Emid, J.H.N. Creyghton, High resolution NMR imaging in solid, Physika B 128 (1985) 81–83.

[2] B.J. Balcom, R.P. MacGregor, S.D. Beyea, D.P. Green, R.L. Armstrong, T.W. Bremner, Single-point ramped imaging with T_1 enhancement (SPRITE), J. Magn. Reson. A 123 (1996) 131–134.

[3] M. Halse, D.J. Goodyear, B. MacMillan, P. Szomolanyi, D. Matheson, B.J. Balcom, Centric scan SPRITE magnetic resonance imaging, J. Magn. Reson. 165 (2003) 219–229.

[4] S.D. Beyea, B.J. Balcom, P.J. Prado, A.R. Cross, C.B. Kennedy, R.L. Armstrong, T.W. Bremner, Relaxation time mapping of short T_2^* nuclei with single-point imaging (SPI) methods, J. Magn. Reson. 135 (1998) 156–164.

[5] L.R. Rabiner, R.W. Schafer, C.M. Rader, The chirp z-transform algorithm and its application, Bell Syst. Tech. J. 48 (1969) 1249–1292.

[6] R. Tong, R.W. Cox, Rotation of NMR images using the 2D chirp z-transform, Magn. Reson. Med. 41 (1999) 253–256.

[7] O. Heid, Sensitivity enhanced single point imaging, Abstract ISMRM (1998) 2186.

[8] M. Halse, J. Rioux, S. Romanzetti, J.B. Kaffanke, B. MacMillan, I. Mastikhin, N.J. Shah, E. Aubanel, B.J. Balcom, Centric scan SPRITE magnetic resonance imaging: optimization of SNR, resolution, and relaxation time mapping, J. Magn. Reson. 169 (2004) 102–117.

[9] J. Rioux, Non-uniform fast Fourier transformation of SPRITE MRI Data, B.CS. Thesis, University of New Brunswick, 2003.

[10] A. Dutt, V. Rokhlin, Fast Fourier transforms for nonequispaced data, SIAM J. Sci. Comput. 14 (1993) 1368–1393.

[11] C.E. Shannon, Communication in the presence of noise, Proc. Inst. Radio Energie 37 (1949) 10–21.

[12] L.I. Bluestein, A linear filtering approach to the computation of the discrete Fourier transform, Northeast Electronics Research and Engineering Meeting Rec. 10 (1968) 218–219.

[13] H.J. Nussbaumer, Fast Fourier Transform and Convolution Algorithms, Springer, 1982.

[14] E.M. Haacke, R.W. Brown, M.R. Thompson, R. Venkatesan, Magnetic Resonance Imaging: Physical Principles and Sequence Design, Wiley, 1999.

[15] F. Natterer, The Mathematics of Computerised Tomography, Teubner, 1986.